Cohesive Zone Finite Element Analysis to Envisage Interface Debonding in AA7020/Titanium Oxide Nanoparticulate Metal Matrix Composites

A. Chennakesava Reddy

Assistant Professor, Department of Mechanical Engineering, MJ College of Engineering and Technology, Hyderabad, India
dr_acreddy@yahoo.com

Abstract: A square array unit cell/2-D rectangular particulate RVE models were used to estimate interface debonding using cohesive zone analysis. The particulate metal matrix composites are titanium oxide/AA7020 alloy at different volume fractions of titanium nitride. Interface debonding was observed in all the composites. The interface debonding occurred between $0^o \le \theta \le 65^o$ in one-fourth model of symmetric geometry of AA7020/TiO_2 composites.

Keywords: AA7020, titanium oxide, rectangular particulate, RVE model, finite element analysis, interface debonding.

1. INTRODUCTION

Cell methods become widely used, which are based on the concept of a Representative Volume Element (RVE). The unit cell methods can easily account for complex microstructural morphology. Furthermore, finite element method is a most straightforward and common method for analyzing and modeling complex structures [1]. Multiphase finite element method is developed for modeling deformation and damage in particle-reinforced composite materials. Interfacial debonding is accommodated by cohesive zone models, in which normal and tangential spring tractions are expressed in terms of interfacial separation [2-15]. The criterion to an interfacial debonding is defined by the maximum normal tensile stress at the nodes of the matrix-inclusion interface. The cohesive zone is considered to be a fracture process zone ahead of the crack tip as illustrated in figure 1 for an infinite plate with a crack. Many different cohesive laws with variances in maximum traction, maximum separation, and shape have been proposed, such as the linear softening cohesive law by Camacho and Ortiz [16], the exponential cohesive law by Needleman [17] and Xu and Needleman [18], the trapezoidal cohesive law by Tvergaard and Huchinson [19], and the polynomial cohesive law by Tvergaard [20].

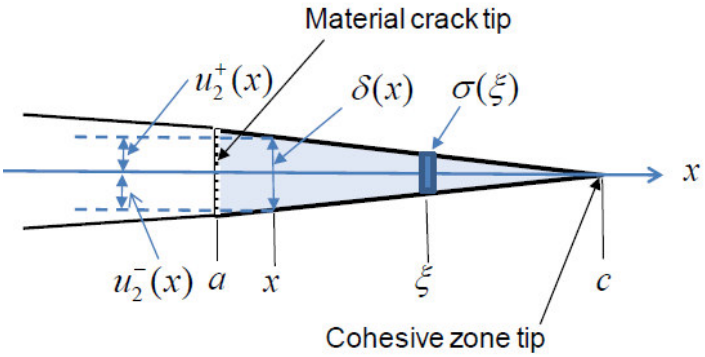

Figure 1: Cohesive traction σ and cohesive zone opening displacement δ.

In the present research, the cohesive zone finite element analysis was carried out to envisage interface debonding in the AA7020/titanium oxide nanoparticulate-reinforced composites. Representative volume elements (RVEs) models were taken from the periodic 2-D rectangular particulates in a square array distribution.

2. MATERIALS AND METHODS

The volume fractions of titanium nitride used in the present work were 10%, 20%, and 30% TiO_2. The matrix material was AA7020 alloy. The periodic model for the representative volume element (RVE) scheme was constructed from 2-D rectangular particulates in a diamond array particulate distribution (figure 2). PLANE183 element was used for the matrix and the

nanoparticulate. The cohesive zone can be incorporated in the continuum formulation by applying the cohesive tractions as boundary conditions. When the discretization is set up, two types of elements are required. One element is a continuum type element and the other a CZM type element. The Newton-Raphson Method (NRM) is used as it supports the concept of a tangent stiffness matrix. The cohesive element is implemented as a linear element with four nodes. The isoparametric formulation is chosen for the element, meaning that shape and displacements are interpolated by the same shape functions. Introducing the natural coordinate system, the linear Lagrangian shape functions are given as:

$$N_1 = \frac{1}{4}(1-\xi)(1-\eta) \qquad N_2 = \frac{1}{4}(1+\xi)(1-\eta)$$
$$N_3 = \frac{1}{4}(1+\xi)(1+\eta) \qquad N_4 = \frac{1}{4}(1-\xi)(1+\eta) \tag{1}$$

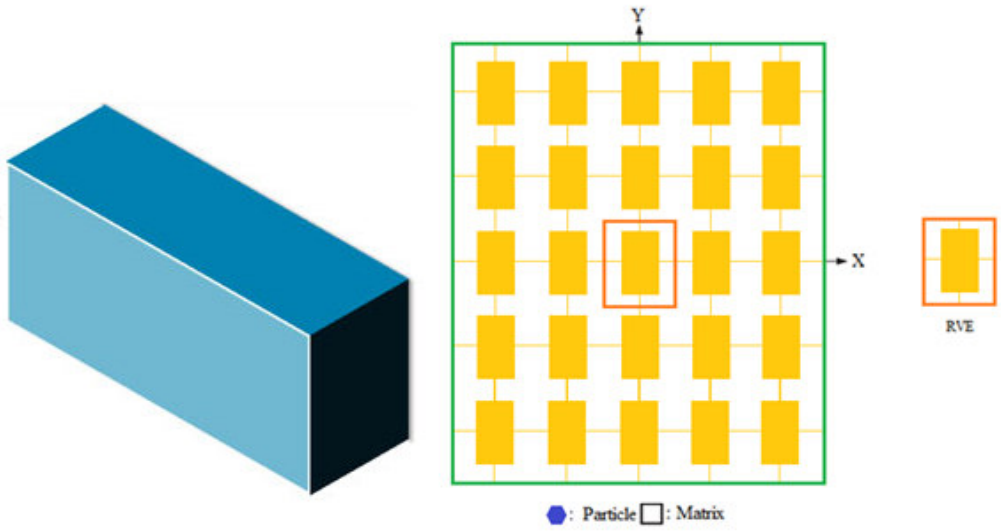

Figure 2: The RVE model: (a) particle distribution and (b) RVE scheme.

Introducing the shape function matrix as:

$$[\mathbf{N}] = \begin{bmatrix} N_1 & 0 & 0 & N_2 & 0 & 0 & N_3 & 0 & 0 & N_4 & 0 & 0 \\ 0 & N_1 & 0 & 0 & N_2 & 0 & 0 & N_3 & 0 & 0 & N_4 & 0 \\ 0 & 0 & N_1 & 0 & 0 & N_2 & 0 & 0 & N_3 & 0 & 0 & N_4 \end{bmatrix} \tag{2}$$

The displacements as functions of the natural coordinates can be written in the matrix-vector form as:

$$\{\mathbf{u}^+\} = [\mathbf{N}]\{\mathbf{q}^+\}$$
$$\{\mathbf{u}^-\} = [\mathbf{N}]\{\mathbf{q}^-\} \tag{3}$$

Shear-log model is based on the assumption that all of the load transfer from matrix to particulate occurs via shear stresses acting on the particulate interface between the two constituents. The rate of change of the stress in the particulate to the interfacial shear stress at that point and the particulate radius, 'r' is given by:

$$\frac{d\sigma_p}{dx} = -\frac{2\tau_i}{r} \tag{4}$$

which may be regarded as the basic shear lag relationship.

The stress distribution in the particulate is determined by relating shear strains in the matrix around the particulate to the macroscopic strain of the composite. Some mathematical manipulation leads to a solution for the distribution of stress at a distance 'x' from the mid-point of the particulate which involves hyperbolic trig functions:

$$\sigma_p = E_p \varepsilon_c [1 - cosh(nx/r) sech(ns)] \tag{5}$$

where ε_c is the composite strain, s is the particulate aspect ratio (length/diameter) and n is a dimensionless constant given by:

$$n = \left[\frac{2E_m}{E_p(1+\nu_m) ln(1+\nu_p)}\right]^{1/2} \tag{6}$$

in which v_m is the Poisson ratio of the matrix. The variation of interfacial shear stress along the particulate length is derived, according to Equation (4), by differentiating this equation, to give:

$$\tau_i = \frac{n\varepsilon_c}{2} E_p sinh\left(\frac{nx}{r}\right) sech(ns) \quad (7)$$

The equation for the stress in the particulate, together with the assumption of a average tensile strain in the matrix equal to that imposed on the composite, can be used to evaluate the composite stiffness. This leads to:

$$\sigma_c = \varepsilon_c \left[v_p E_p \left(1 - \frac{tanh(ns)}{ns}\right) + (1 - v_p) E_m\right] \quad (8)$$

The expression in square brackets is the composite stiffness. The stiffness is a function of particulate aspect ratio, particulate/matrix stiffness ratio and particulate volume fraction.

If the particle deforms in an elastic manner (according to Hooke's law) then,

$$\tau = \frac{n}{2}\sigma_p \quad (9)$$

If particle fracture occurs when the stress in the particulate reaches its ultimate tensile strength, $\sigma_{p,uts}$, then setting the boundary condition at

$$\sigma_p = \sigma_{p,\,uts} \quad (10)$$

and substituting into Equation (9) gives a relationship between the strength of the particle and the interfacial shear stress such that if

$$\sigma_{P,uts} < \frac{2\tau}{n} \quad (11)$$

Then the particle will fracture. Similarly if interfacial debonding/yielding is considered to occur when the interfacial shear stress reaches its shear strength

$$\tau = \tau_{max} \quad (12)$$

For particle/matrix interfacial fracture can be established whereby,

$$\tau_{max} < \frac{n\sigma_p}{2} \quad (13)$$

This approach suggests that the outcome of a matrix crack impinging on an embedded particle depends on the balance between the particle strength and the shear strength of the interface.

For plane strain conditions, the macro stress- macro strain relation is as follows:

$$\begin{Bmatrix} \overline{\sigma_x} \\ \overline{\sigma_y} \\ \overline{\tau_{xy}} \end{Bmatrix} = \begin{bmatrix} \overline{C_{11}} & \overline{C_{12}} & 0 \\ \overline{C_{21}} & \overline{C_{22}} & 0 \\ 0 & 0 & \overline{C_{33}} \end{bmatrix} \times \begin{Bmatrix} \overline{\varepsilon_x} \\ \overline{\varepsilon_y} \\ \overline{\gamma_{xy}} \end{Bmatrix} \quad (14)$$

The interfacial tractions can be obtained by transforming the micro stresses at the interface as given in Eq. (3):

$$t = \begin{Bmatrix} t_z \\ t_n \\ t_t \end{Bmatrix} = T\sigma \quad (15)$$

where, $T = \begin{bmatrix} 0 & 0 & 0 \\ cos^2\theta & sin^2\theta & 2sin\theta cos\theta \\ -sin\theta cos\theta & sin\theta cos\theta & cos^2\theta - sin^2\theta \end{bmatrix}$

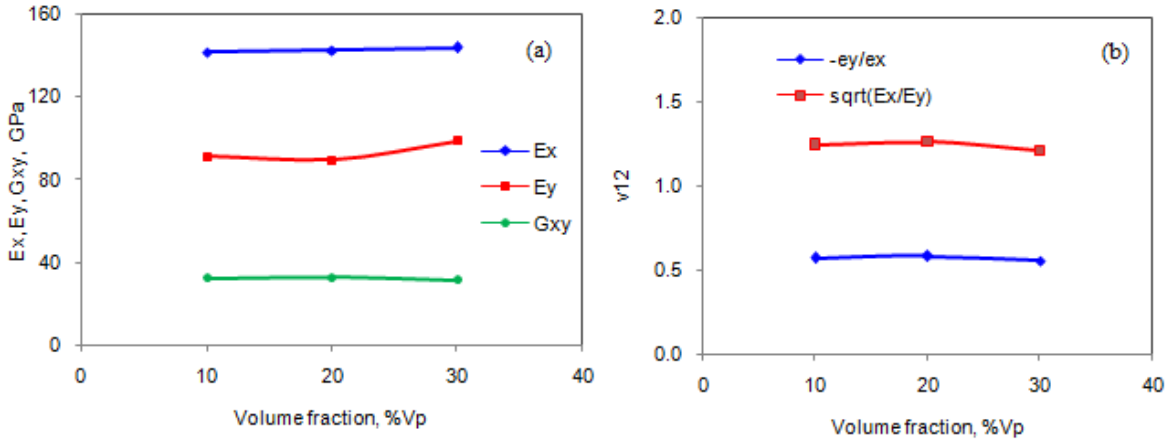

Figure 3: Effect of volume fraction on effective material properties.

3. RESULTS AND DISCUSSION

The tensile modulus increased (141.76 < 142.62 < 143.83 GPa) with volume fraction of titanium oxide (TiO_2) as shown figure 3a. Compression modulus was, respectively, 91.46 GPa, 89.69 GPa and 98.62 of AA7020/10% TiO_2, AA7020/20% TiO_2 and AA7020/30% TiO_2 composites; whereas shear modulus was, respectively, 32.34 GPa, 32.60 GPa and 31.56 of AA7020/10% TiO_2, AA7020/20% TiO_2 and AA7020/30% TiO_2 composites. The major Poisson's ratio decreased with increase of volume fractions of TO_2 (figure 3b). The difference in the elastic moduli of TiO_2 particulates and AA7020 alloy matrix is 216 GPa. The Poisson's ratios of AA7020 alloy matrix and TiO_2 particulates are, respectively, 0.33 and 0.29.

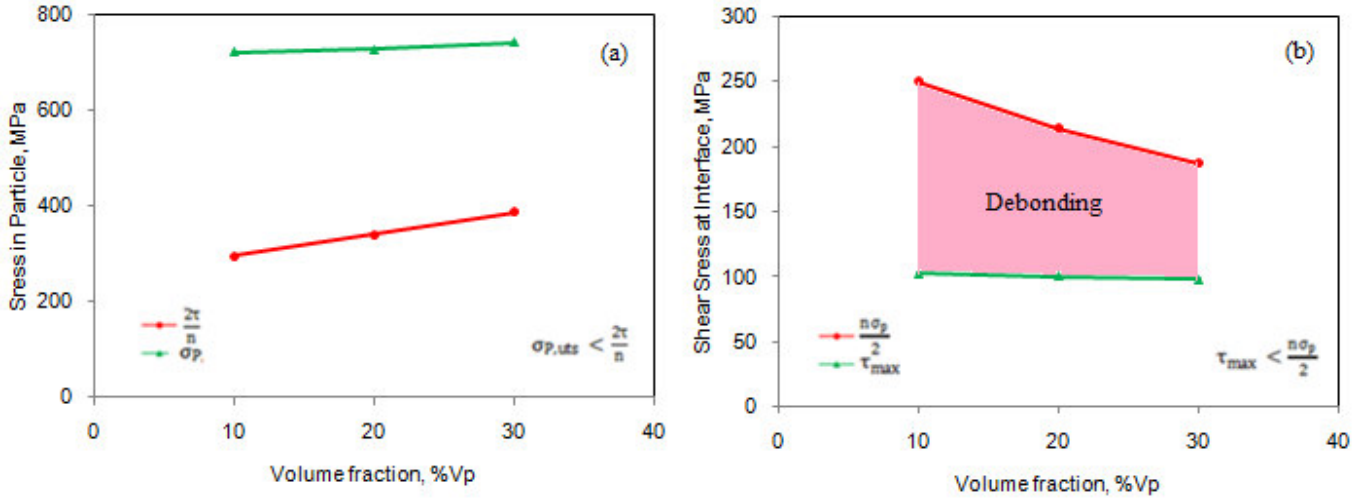

Figure 4: Fracture criteria of: (a) particulate fracture and (b) interface debonding.

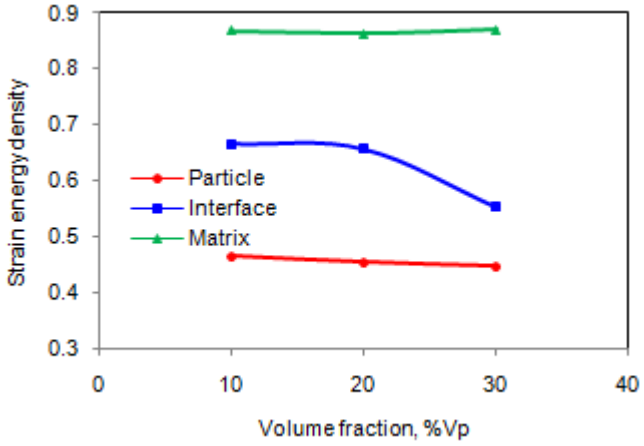

Figure 5: Effect of volume fraction on strain energy density.

The TiO_2 particulate fracture was not exposed in the AA7020/TiO_2 composites as shown in figure 4a. The TiO_2 particulate fracture was not produced as the condition $\sigma_p \leq 2\tau/n$ did not satisfied. The condition $\tau_{max} < n\sigma_p/2$ satisfied for the occurrence of debonding in the composites including 10%, 20% and 30% TiO_2 (figure 4b). The strain energy density decreased at the interface with an increase in the volume fraction of TiO_2. Also, the strain energy density of TiO_2 decreased in the composites. This represents the debonding tendency at the interface between AA7020 alloy matrix and TiO_2 nanoparticulates. The decreased strain energy density attributes to the interface debonding. The strain energy density in the TiO_2 nanoparticulates was lower than that developed in the matrix and at the interface. The normal and tangential tractions are plotted in figure 6a. Because of symmetry considerations, the variations of the interface stresses with circumferential location are plotted only for the range $0^o \leq \theta \leq 90^o$. For AA7020/30%$TiO_2$ composites, the normal tractions are higher than that for AA7020/10%TiO_2 and AA7020/20%TiO_2 composites (figure 6a). These results can be interpreted that the particulates are far enough apart at 10% particulate fiber volume fraction. This means that they do not interact (i.e., any particular particulate does not feel the influence of the other particulates in the neighborhood). At 10% particulate fiber volume fraction of TiO_2 the particulates are close

enough together that any individual particulate feels the influence of neighboring particulates. The interface debonding occurred between $0^o \leq \theta \leq 65^o$. The normal and tangential displacements are also plotted in figure 6b. The normal and tangential displacements are higher for AA7020/30%TiO_2 composites than those for AA7020/10%TiO_2 and AA7020/20%TiO_2 composites.

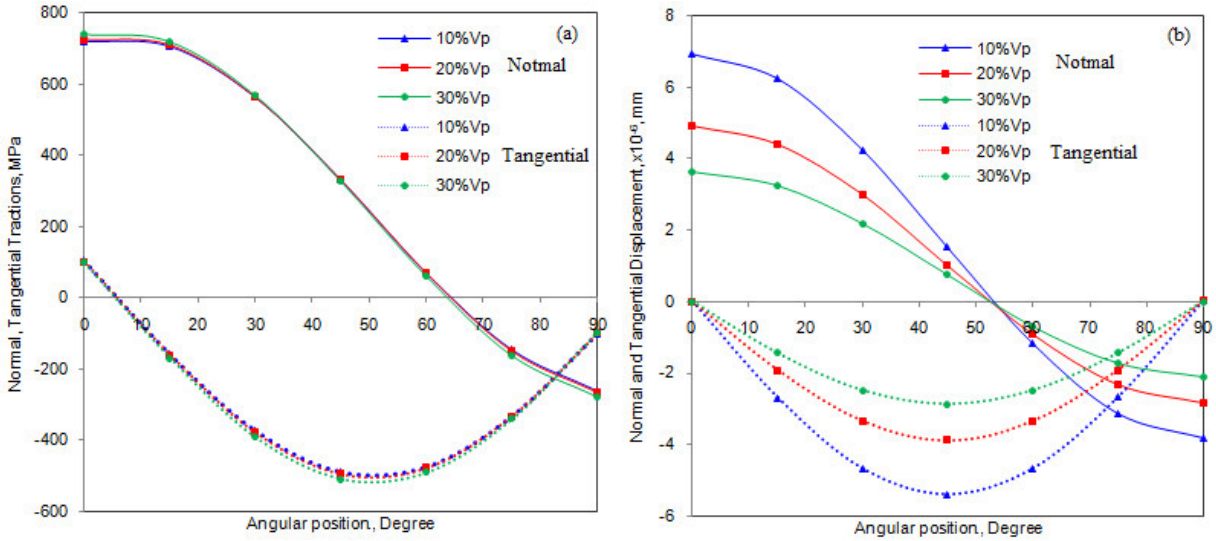

Figure 6: Normal and tangential: (a) tractions and (b) displacements.

As the raster images (figure 7) obtained from finite element analysis, the interface debonding is highest in AA7020/30%TiO_2 composites. The images (figure 8) obtained from the scanning electron microscopy confirm the results obtained from the finite element analysis. The areas representing 'A' are the debonding zones and "B" represents the tear bands TiO_2 particulates.

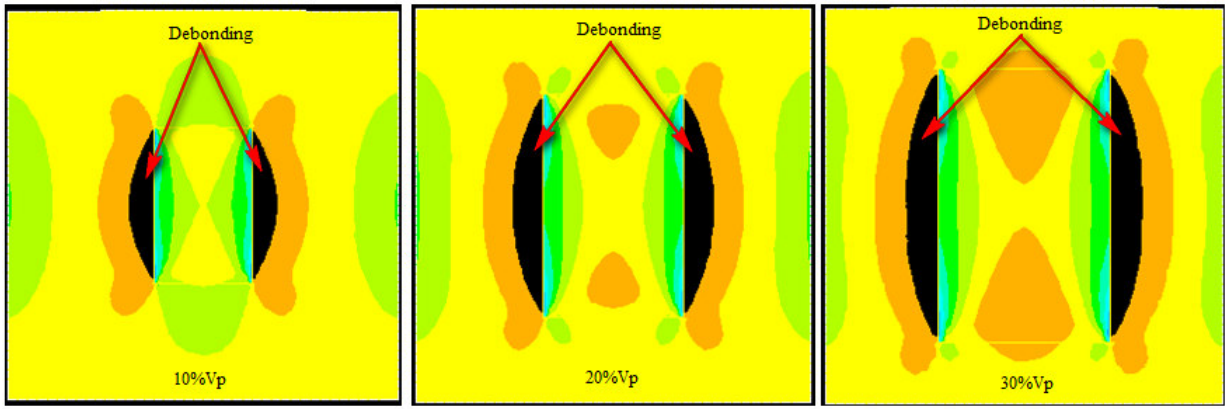

Figure 7: Results of cohesive zones obtained from finite element analysis for debonding.

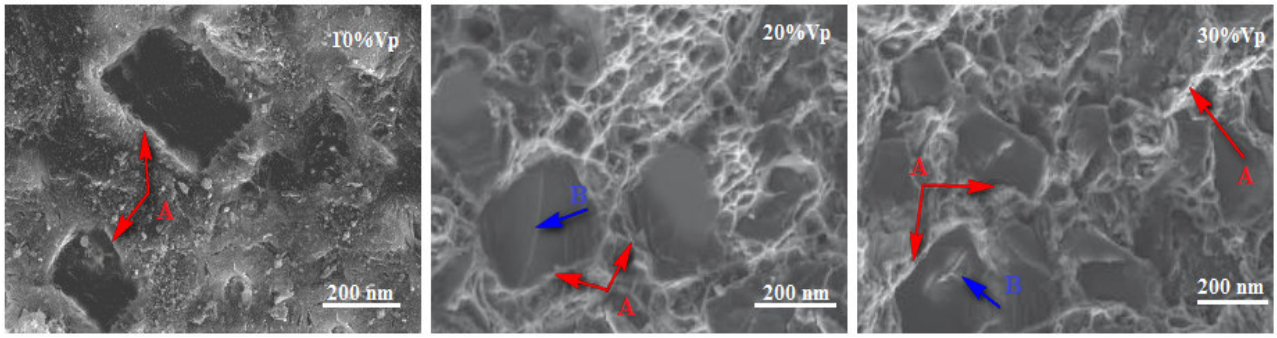

Figure 8: SEM images illustrating interface debonding (A) and tear bands (B) in the TiO_2 particulates.

4. CONCLUSION

The interface debonding occurred in the composites containing 10% , 20% and 30% volume fractions TiO_2.; Nanoparticulate damage had not occurred. The interface debonding increased with an increase of volume fractions of TiO_2 in the composites. The interface debonding occurred between $0^o \leq \theta \leq 65^o$ in one-fourth model of symmetric geometry of AA7020/TiO_2 composites.

REFERENCES

1. T. Steinkopff and M. Sautter, Simulating the elasto-plastic behavior of multiphase materials by advanced finite element techniques Part I: a rezoning technique and the multiphase element method, Computational Materials Science, 4, 1995, pp.10–14
2. A. Chennakesava Reddy, Assessment of Debonding and Particulate Fracture Occurrences in Circular Silicon Nitride Particulate/AA5050 Alloy Metal Matrix Composites , National Conference on Materials and Manufacturing Processes, Hyderabad, India, 27-28 February1998, pp.104-109.
3. B. Kotiveera Chari and A. Chennakesava Reddy, Numerical Simulation of Particulate Fracture in Round Silicon Nitride Particulate/AA6061 Alloy Metal Matrix Composites, National Conference on Materials and Manufacturing Processes, Hyderabad, India, 27-28 February 1998, pp. 110-114.
4. H. B. Niranjan and A. Chennakesava Reddy, Effect of Elastic Moduli Mismatch on Particulate Fracture in AA7020/Silicon Nitride Particulate Metal Matrix Composites , National Conference on Materials and Manufacturing Processes, Hyderabad, India, 27-28 February, 115-118, 1998
5. P. Martin Jebaraj and A. Chennakesava Reddy, Cohesive Zone Modelling for Interface Debonding in AA8090/Silicon Nitride Nanoparticulate Metal Matrix Composites, National Conference on Materials and Manufacturing Processes, Hyderabad, India, 27-28 February 1998, pp. 119-122.
6. P. Martin Jebaraj and A. Chennakesava Reddy, Plane Strain Finite Element Modeling for Interface Debonding in AA1100/Silicon Oxide Nanoparticulate Metal Matrix Composites, National Conference on Materials and Manufacturing Processes, Hyderabad, India, 27-28 February 1998, pp. 123-126.
7. A. Chennakesava Reddy, Local Stress Differential for Particulate Fracture in AA2024/Titanium Carbide Nanoparticulate Metal Matrix Composites, National Conference on Materials and Manufacturing Processes, Hyderabad, India, 27-28 February 1998, pp. 127-131.
8. B. Kotiveera Chari and A. Chennakesava Reddy, Interface Debonding and Particulate Facture based on Strain Energy Density in AA3003/MgO Nanoparticulate Metal Matrix Composites, National Conference on Materials and Manufacturing Processes, Hyderabad, India, 27-28 February 1998, pp. 132-136.
9. H. B. Niranjan and A. Chennakesava Reddy, Numerical and Analytical Prediction of Interface Debonding in AA4015/Boron Nitride Nanoparticulate Metal Matrix Composites , National Conference on Materials and Manufacturing Processes, Hyderabad, India, 27-28 February 1998, pp. 137-140.
10. S. Sundara Rajan and A. Chennakesava Reddy, Effect of Particulate Volume Fraction on Particulate Cracking in AA5050/Zirconium Oxide Nanoparticulate Metal Matrix Composites , National Conference on Materials and Manufacturing Processes, Hyderabad, India, 27-28 February 1998, pp. 156-159.
11. S. Sundara Rajan and A. Chennakesava Reddy, Cohesive Zone Analysis for Interface Debonding in AA6061/Titanium Nitride Nanoparticulate Metal Matrix Composites , National Conference on Materials and Manufacturing Processes, Hyderabad, India, 27-28 February 1998, pp. 160-164.
12. A. Chennakesava Reddy, Effect of Particle Loading on Microealstic Behavior and interfacial Tractions of Boron Carbide/AA4015 Alloy Metal Matrix Composites, 1st International Conference on Composite Materials and Characterization, Bangalore, 14-15 march 1997, pp. 176-179.7
13. A. Chennakesava Reddy, Reckoning of Micro-stresses and interfacial Tractions in Titanium Boride/AA2024 Alloy Metal Matrix Composites, 1st International Conference on Composite Materials and Characterization, Bangalore, 14-15 march 1997, pp. 195-197.
14. A. Chennakesava Reddy, Interfacial Debonding Analysis in Terms of Interfacial Tractions for Titanium Boride/AA3003 Alloy Metal Matrix Composites, 1st National Conference on Modern Materials and Manufacturing , Pune, India, 19-20 December 1997, pp. 124-127.
15. A. Chennakesava Reddy, Evaluation of Debonding and Dislocation Occurrences in Rhombus Silicon Nitride Particulate/AA4015 Alloy Metal Matrix Composites, 1st National Conference on Modern Materials and Manufacturing , Pune, India, 19-20 December 1997, pp. 278-282.
16. G.T. Camacho, and M. Ortiz, Computational modeling of impact damage in brittle materials, International Journal of Solids and Structures, 33, 1996, pp. 2899–2938.
17. A. Needleman, A continuum model for void nucleation by inclusion debonding, ASME Journal of Applied Mechanics, 54, 1987, pp. 525–531.
18. X. P. Xu, and A. Needleman, Void nucleation by inclusions debonding in a crystal matrix, Modelling and Simulation in Materials Science and Engineering, 1, 1993, pp. 111–132.
19. V. Tvergaard, and J. W. Hutchinson, The relation between crack growth resistance and fracture process parameters in elastic–plastic solids, Journal of the Mechanics and Physics of Solids, 40, 1992, pp. 1377–1397.
20. V. Tvergaard, Effect of fibre debonding in a whisker-reinforced metal, Materials Science and Engineering A, 125, 1990, pp. 203–213.